

# *Characterisation of the bending stiffness components of MDF panels from full-field slope measurements*

**J. Xavier, U. Belini, F. Pierron, J. Morais,  
J. Lousada & M. Tomazello**

**Wood Science and Technology**  
Journal of the International Academy of  
Wood Science

ISSN 0043-7719

Volume 47

Number 2

Wood Sci Technol (2013) 47:423–441

DOI 10.1007/s00226-012-0507-6



**Your article is protected by copyright and all rights are held exclusively by Springer-Verlag Berlin Heidelberg. This e-offprint is for personal use only and shall not be self-archived in electronic repositories. If you wish to self-archive your work, please use the accepted author's version for posting to your own website or your institution's repository. You may further deposit the accepted author's version on a funder's repository at a funder's request, provided it is not made publicly available until 12 months after publication.**

# Characterisation of the bending stiffness components of MDF panels from full-field slope measurements

J. Xavier · U. Belini · F. Pierron · J. Morais ·  
J. Lousada · M. Tomazello

Received: 4 October 2011 / Published online: 4 October 2012  
© Springer-Verlag Berlin Heidelberg 2012

**Abstract** This paper deals with the characterisation of bending stiffness components of medium density fibreboard (MDF) by carrying out a single plate bending test. The approach couples full-field slope measurements with an inverse identification method. MDF panels manufactured with different fractions of *Eucalyptus* fibres and sugarcane bagasse particles were used. The slope maps generated across the plate surface were measured by the deflectometry technique. The curvature fields of the deformed plate were reconstructed by numerical differentiation afterwards. The virtual fields method was then implemented for material parameter identification under the framework of Kirchhoff–Love plate bending theory. The elastic properties obtained from the proposed data reduction (i.e. simultaneous identification of modulus of elasticity, *Poisson's* ratio and shear modulus) were compared with values determined from classical three-point bending tests and reported in the literature. The set of properties were found in relatively good agreement.

## Introduction

In the last decades, developments on both manufacturing processes and wood adhesives have led to new engineering wood products (e.g. veneer, particle or fibre-

---

J. Xavier (✉) · J. Morais · J. Lousada  
CITAB/UTAD, Engenharias I, Apartado 1013, 5001-801 Vila Real, Portugal  
e-mail: jmcx@utad.pt

U. Belini · M. Tomazello  
Departamento de Ciências Florestais, ESALQ/USP, Av. Pádua Dias, 11,  
São Paulo, Piracicaba CEP 13418-900, Brazil

F. Pierron  
LMPF, Arts et Métiers ParisTech, Châlons-en-Champagne, France

based products) (Williamson 2002). These materials have been designed to fulfil specific structural requirements and are emerging in different applications. An important class of these wood products is the medium density fibreboard (MDF). Conventionally, MDF panels are produced from wood-based raw material by transforming wood chips into fibres (refining system) and gluing them with a resin binder by applying high temperature and pressure. However, alternative sources of lignocellulose fibres in the MDF manufacturing process have been explored, namely by using agricultural and forestry waste, in a policy of better preservation and management of the available natural resources. The material tested in this work was MDF consisting of a mixture of sugarcane bagasse (*Saccharum* spp.) particles—residue resulting from sugar-alcohol mills—together with *Eucalyptus grandis* fibres obtained in industrial refiner system (Belini et al. 2012). This MDF product requires specific mechanical characterisation. Standard test methods for mechanical characterisation of wood products only specify the determination of the modulus of elasticity and modulus of rupture by three-point bending tests (EN 310 1993).

Full-field optical methods of displacement and strain measurements are being increasingly used in experimental solid mechanics (Grédiac 2004). According to the physical phenomenon involved in the measurement, these techniques can be divided into white-light techniques (e.g. digital image correlation and grid methods) and interferometric techniques (e.g. speckle and moiré interferometry and shearography). In contrast to strain gauges or extensometers, these methods provide full-field data and are contact-free. Following the development of optical techniques in the last decades, novel identification methods have been proposed for material parameters based on full-field measurements. A survey of these methods can be found in Avril et al. (2008). This approach offers several advantages over classical data reduction, such as multi-parameter identification from a single-test configuration.

In this work, a plate bending test was proposed for direct identification of the whole set of bending stiffness components of MDF panels. The test method consists in gripping the plate at several points at the edges and applying a point load at a given location on the plate. The heterogeneous slope fields observed at the surface of the plate were measured by the deflectometry technique (Surrel 2004). An experimental procedure was proposed for transferring a reflective coating to the MDF panels, required in this technique. The curvature fields of the deformed plate were then reconstructed by numerical differentiation. Finally, the virtual fields method was implemented for material parameter identification within the framework of the Kirchhoff–Love thin plate theory (Grédiac et al. 2003). This is an inverse identification method from which the whole set of active material parameters can be retrieved from full-field measurements on a single test.

### Full-field slope measurements

In a plate bending test, the mechanical response is governed by bending stiffness components relating bending moments to curvatures. According to the classical plate theory (Kirchhoff–Love theory), the deformation of the plate can be described by the deflection of its mid-plane surface. Both white-light and interferometric

techniques exist for measuring the out-of-plane full-field displacement of an object, such as stereovision (Xavier et al. 2012) or electronic speckle pattern interferometry (ESPI) (Müller et al. 2005). It is worth noticing that in-plane displacements could be directly measured with these techniques, but their amplitude is very small, typically one to two orders of magnitude lower than the in-plane ones, which makes them extremely difficult to measure directly (e.g. see Pierron 2009). These techniques differ in terms of experimental set-up and performance (accuracy and sensitivity), but the main disadvantage resides in the second numerical differentiation of the out-of-plane displacement, since this computation process dramatically amplifies the noise in the reconstructed fields. In order to avoid this major drawback, the slope field (first derivative of the deflection) can be directly measured experimentally by the deflectometry technique (Surrel 2004). In the following, a summary of the deflectometry technique is presented.

### Deflectometry technique

The photo-mechanical set-up of the deflectometry technique coupled with a plate bending test is schematically represented in Fig. 1. The deflectometry technique is a non-interferometric optical method that provides the measurement of the local slope ( $\alpha$ ) of the deformed plate by means of the apparent displacement ( $u$ ) of the grid imaged by reflection through the plate surface. It is therefore necessary that the surface of interest has a sufficient specular reflection such that the grid image, reflected over the plate surface, can be formed and recorded with suitable contrast and rectilinearity. In the configuration of Fig. 1a, although the reflected image will change as a function of both deflection and slope of the plate, the reflection will be mostly influenced by the local rotation of the plate (it is assumed that the deflection remains small and no rigid-body out-of-plane displacements exist). The grid consists of a periodic pattern of dark and bright lines, characterised by a spatial frequency vector which magnitude is the inverse of the grid pitch ( $p$ ). A crossed (horizontal and vertical) grid can be used for measuring the two components of slope field along the directions defined by the grid lines. At least two images of the grid are taken before and after deformation. With the grid method, it can be shown that the difference of phase ( $\Delta\phi$ ) is proportional to the displacement of the grid image according to the following relationship

$$u_{\beta}(x_1, x_2) = \frac{2\pi}{p} \Delta\phi_{\beta}(x_1, x_2) \quad (1)$$

where  $\beta = 1$  or 2, respectively, for horizontal (vertical lines) or vertical (horizontal lines) components of the displacement.

A given small area (point)  $P$  of the plate which is imaged by a pixel  $O$  on the camera sensor (Fig. 1a) is considered. In the undeformed configuration, the light intensity reflected at  $P$  will come from the geometrical point  $M$  of the grid (law of reflection). The plate is then deformed by an external bending moment, and a local rotation ( $\alpha$ ) of the plate section is assumed at point  $P$ . From the law of reflection, it can be concluded that this rotation of the plate is actually equivalent to a displacement of the grid image by a magnitude defined by the geometrical rotation

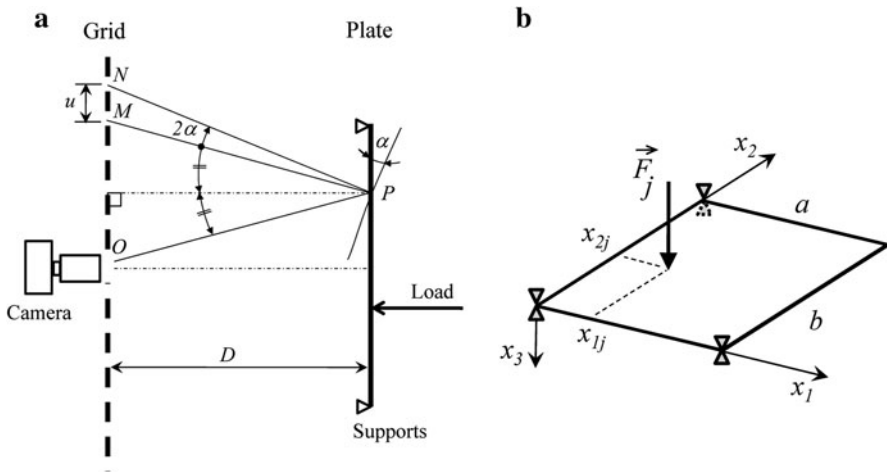


**Fig. 1** Schematic representation of **a** deflectometry technique coupled with **b** plate bending test

of  $2\alpha$  (Fig. 1a). At the pixel of the camera sensor, this rotation is recorded as a light intensity variation, since the light reflected at point  $P$  comes from point  $N$  of the grid in the deformed configuration. Thus, the phase variation in the grid images encodes the local slope of the deformed plate. It is considered that the grid-plate distance ( $D$ ) is significantly greater than the deflection ( $w$ ) generated by the bending load ( $D \gg w \rightarrow \tan \theta \approx \theta$ ) (Fig. 1a). In a first-order approximation, it can be demonstrated (Kim 2008) that the apparent displacement of the grid image ( $u$ )—from point  $M$  to point  $N$  in the grid plane—is related to the local slope of the plate ( $\alpha$ ) by

$$u_{\beta}(x_1, x_2) \approx 2D\alpha_{\beta}(x_1, x_2). \quad (2)$$

Combining Eqs. (1) and (2), the slope can then be given as a function of the phase difference as

$$\alpha_{\beta}(x_1, x_2) = \frac{p}{4\pi D} \Delta\phi_{\beta}(x_1, x_2). \quad (3)$$

The sensitivity ( $s$ ) of the method (defined as the ratio between phase variation and local slope) is then given by  $s = 4\pi D/p$ . Depending on the application, the sensitivity can be adjusted either by the grid-plate distance ( $D$ ) or by the pitch of the grid ( $p$ ). Moreover, the spatial resolution (minimum distance separating two independent measurement points) and resolution (the smallest measured value that can be detected) associated with deflectometry technique can be adjusted separately by setting  $p$  and  $D$ , respectively. Outstanding features of the deflectometry technique are the relatively simple set-up, the basic optical equipment required and the large range of accessible length scales (from small specimens up to structural members). However, the main drawback remains the fact that the surface of interest must have a mirror-like characteristic and that it is presently restricted to flat surfaces (although it might be possible to extend it to moderately curved surfaces).

## Identification method

Novel identification methods have been proposed for material parameter characterisation based on full-field measurements (Avril et al. 2008). In this work, the virtual fields method (VFM) was used (Pierron and Grédiac 2012). It is well adapted to process full-field measurements due to its integral formulation and can provide a direct solution of the unknown constitutive parameters in the case, for instance, of linear elasticity. The principle of this method applied to a plate bending test is presented in the following.

### Virtual fields method for plate bending problem

#### Principle

The virtual fields method is based on the principle of virtual work (PVW). In the absence of body forces and under static conditions, the PVW can be written as

$$-\int_V \sigma : \varepsilon^* dV + \int_S \mathbf{T} \cdot \mathbf{u}^* dS = 0 \quad (4)$$

where  $\sigma$  is the Cauchy stress tensor,  $\varepsilon^*$  is the virtual strain tensor,  $\mathbf{T}$  is the vector of external surface tractions applied over the solid boundary  $S$  and  $\mathbf{u}^*$  is the virtual displacement vector. In developing the VFM, a constitutive law for the material behaviour must be assumed a priori. In this work, the Kirchhoff–Love plate bending theory was considered. In this case, the displacement and strain fields in the plate are linear functions of first and second partial derivatives of the deflection field ( $u_3(x_1, x_2)$ ), respectively. In a plate bending problem, the stress components ( $\{\sigma\}$ ) are integrated over the thickness of the plate ( $h$ ) defining bending moment resultants ( $\{M\}$ ), whilst the strain components ( $\{\varepsilon\}$ ) are given as functions of the curvature fields of the plate ( $\{K\}$ ). It is assumed hereafter that the material is homogeneous through the thickness. Although the MDF plate has an inherent density variation through the thickness resulting from the manufacturing process (Zhou et al. 2011), it will be considered, in a first approximation, that this hypothesis is reasonable. In this work, the PVW will be written in bending

$$\int_S \{M\}^T \{K^*\} dS = \sum_{j=1}^n F_j u_{3,j}^* \quad (5)$$

where  $n$  represents the number of external point loads ( $F_j$ ) applied to the plate (Fig. 1b). The bending moment–curvature constitutive equation is chosen for an isotropic homogeneous material:  $\{M\} = [D]\{K\}$ , where  $[D]$  is the bending stiffness matrix. By placing this constitutive equation into the PVW for plate bending problem (Eq. 5), the following equation is obtained

$$\int_S \{K\}^T [D] \{K^*\} dS = \sum_{j=1}^n F_j u_{3j}^* \quad (6a)$$

where  $\{M\}^T = \{K\}^T [D]$  since  $[D]$  is symmetrical. In this paper, it will be assumed that the plates have an isotropic behaviour in bending. This assumption will be checked a posteriori (see Eq. 9). It should be noted that the present approach can be extended to anisotropic elasticity (Kim 2008). Thus, by developing Eq. (6a) for an isotropic material

$$\begin{aligned} D_{11} \int_S \left( K_{11} K_{11}^* + K_{22} K_{22}^* + \frac{1}{2} K_{12} K_{12}^* \right) dS \\ + D_{12} \int_S \left( K_{11} K_{22}^* + K_{22} K_{11}^* + \frac{1}{2} K_{12} K_{12}^* \right) dS = \sum_{j=1}^n F_j u_{3j}^*. \end{aligned} \quad (6b)$$

In Eq. (6a), the unknown bending stiffness components ( $D_{ij}$ ) are expressed as a function of the measured curvature fields ( $K_{ij}$ ) and applied load ( $F_j$ ) as well as virtual deflection ( $u_{3j}^*$ ) and curvature ( $K_{ij}^*$ ) fields. The VFM consists in writing Eq. (6b) with as many kinematic admissible virtual fields as unknown constitutive parameters. This procedure leads to a linear system of equation

$$\begin{bmatrix} I_{11}^{(1)} & I_{12}^{(1)} \\ I_{11}^{(2)} & I_{12}^{(2)} \end{bmatrix} \begin{bmatrix} D_{11} \\ D_{12} \end{bmatrix} = \sum_{j=1}^n F_j \begin{bmatrix} u_{3j}^{*(1)}(x_1, x_2) \\ u_{3j}^{*(2)}(x_1, x_2) \end{bmatrix} \quad (7)$$

which can be solved for identifying the bending stiffness components provided that heterogeneous curvatures fields are measured over the plate and the virtual fields ( $u_{3j}^{*(k)}, K_{ij}^{*(k)}$  with  $k = 1, 2$ ) are linearly independent.

### Choice of virtual fields

The virtual fields figuring in the linear system of Eq. (7) are mathematical functions ( $u_3^*$  must be of class  $C^0$ ) which must satisfy the constraints at boundary conditions of the body (kinematically admissible). These functions can be selected either intuitively (a priori choice) or by some automatic process (Grédiac et al. 2003). Polynomial and finite element basis functions have been proposed for automatically generating the virtual fields (Grédiac et al. 2006). Since a large number of possible virtual fields exist, a constrained optimisation scheme has also been proposed for selecting virtual fields that minimise the sensitivity of the VFM to noise (maximum likelihood solution) (Avril et al. 2004). Such strategy was found to significantly improve the robustness of the method.

In a first approach, the virtual fields used in this work were defined intuitively. For simplicity, constant curvature virtual fields were selected as summarised in Table 1. These virtual fields are kinematically admissible with regard to the plate bending problem illustrated in Fig. 1b, where the plate is fixed at points  $P_1(0,0)$ ,



$P_2(a, 0)$  and  $P_3(0, b)$ . For the resolution of Eq. (7), virtual fields 1 and 2 (Table 1) can be selected, leading to the following linear system of equations

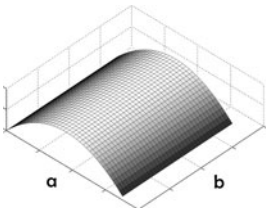
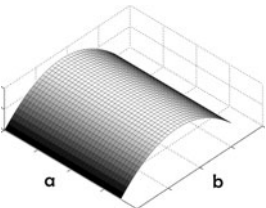
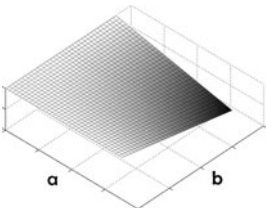
$$\begin{bmatrix} \int_S K_{11} dS & \int_S K_{22} dS \\ \int_S K_{22} dS & \int_S K_{11} dS \end{bmatrix} \begin{bmatrix} D_{11} \\ D_{12} \end{bmatrix} = - \sum_{j=1}^n F_j \begin{bmatrix} \frac{x_{1j}}{2} (x_{1j} - a) \\ \frac{x_{2j}}{2} (x_{2j} - b) \end{bmatrix}. \quad (8)$$

The integrals in Eq. (8) were approximated by the rectangular rule:  $\int_S K_{ij} dS = \sum_{k=1}^m K_{ij}^{(k)} s^{(k)} \approx S \bar{K}_{ij}$ , where  $S$  represents the surface of the plate and  $\bar{K}_{ij} = (1/m) \sum_{k=1}^m K_{ij}^{(k)}$ . Equation (8) allows the identification of the whole set of bending stiffness components from a single plate bending test by properly choosing a point loading case:  $F_1(x_{1j}, x_{2j}) (j = n = 1)$  (Fig. 1b). Besides, the redundancy of a third equation given by the twisting virtual field 3 (Table 1) can be used to verify the isotropy of the MDF plate assumed a priori in the chosen constitutive law. Accordingly, an independent evaluation of  $D_{66} = (D_{11} - D_{12})/2$  can be obtained by choosing a second load case  $F_2(x_{12}, x_{22})$

$$D_{66} = - \frac{F_2}{2 \int_S K_{12} dS} x_{12} x_{22} \quad (9)$$

with  $x_{12} \neq 0$  and  $x_{22} \neq 0$ . Experimentally, to solve both Eqs. (8) and (9), the plate bending test can be performed twice by considering two independent loading cases on the same MDF plate. Generally speaking, the first loading case can lead to the full identification of the bending stiffness matrix, whilst the second loading case gives an independent verification of the isotropy assumption. This complementary test can be used, for instance, to check the random orientation of the fibres following the MDF manufacturing process.

**Table 1** Selection of virtual fields

Virtual fields 1	Virtual fields 2	Virtual fields 3
Curvature fields: $K_{11}^{*(1)} = 1$ , $K_{22}^{*(1)} = K_{12}^{*(1)} = 0$	Curvature fields: $K_{22}^{*(2)} = 1$ , $K_{11}^{*(2)} = K_{12}^{*(2)} = 0$	Curvature fields: $K_{12}^{*(3)} = 1$ , $K_{11}^{*(3)} = K_{22}^{*(3)} = 0$
Deflection fields: $u_3^{*(1)} = -\frac{x_1}{2} (x_1 - a)$	Deflection fields: $u_3^{*(2)} = -\frac{x_2}{2} (x_2 - b)$	Deflection fields: $u_3^{*(3)} = -\frac{x_1 x_2}{2}$
		

## Experimental work

### Medium density fibreboard panels

The MDF panels tested in this work consisted of a mixture of *Saccharum* spp. bagasse particles and *Eucalyptus* fibres. This new MDF was intended to represent a low-cost fibrous raw material panel by incorporating waste sugarcane bagasse in combination with *Eucalyptus* fibre, a raw material normally used in Brazil for fibreboard manufacturing. Bagasse particles collected from sugarcane culms were used in the panel manufacturing. Fibre samples of *Eucalyptus grandis* wood were collected after refining of the wood chips in an industrial apparatus.

The raw material was dried (70 °C; 2–3 % moisture content) and weighed in different fractions according to treatments summarised in Table 2. The bagasse particles and *Eucalyptus* fibres were then transferred to the glue-system compartment, and urea formaldehyde resin and wax emulsion were sprayed using spray nozzles. The fibre-mass was manually laid out in a wooden box placed in an aluminium plate. Manual pressure was applied through the box cover. The fibres-mat was then pressed in a laboratory press by progressively increasing the pressure level at constant temperature of 190 °C. The fibre panel was then cooled to room temperature. At the end of the manufacturing process, the MDF panels were cut at nominal dimensions of  $370 \times 370 \times 15 \text{ mm}^3$ . The density of these panels was about  $750 \text{ kg/m}^3$ . For the mechanical characterisation, three panels per treatment (total of 46 panels) were selected for standard three-point bending tests, whilst one panel per treatment (total of 12 panels) was used for the proposed plate bending test based on full-field slope measurements.

### Three-point bending test method

The MDF panels (Table 2) were characterised by means of three-point bending tests (EN 310 1993). For each manufactured panel, four specimens with nominal dimensions of  $350(l) \times 50(b) \times 15(h) \text{ mm}^3$  were cut. Twelve specimens per treatment (Table 2) were tested in a total of 144 tests. The mechanical set-up of the three-point bending test is shown in Fig. 2. Tests were carried out with a cross-head displacement rate of 1 mm/min. The load ( $F$ ) was measured by means of a load cell of 5 kN. The span ( $L$ ) between supports was 300 mm. The Euler–Bernoulli bending theory was assumed for determining the modulus of elasticity according to the following equation

$$E = \frac{1}{4b} \left( \frac{L}{h} \right)^3 \frac{F}{u_3} \quad (10)$$

where  $u_3$  is the deflection measured as the displacement of the cross-head of the test machine. The stiffness  $F/u_3$  was determined from the initial portion of the load–deflection curve by least-squares fit of a straight line.

**Table 2** Composition of MDF panels and treatments

Treatment (No)	Resin content (%)	Wax (%)	Raw material		Thickness	
			<i>Eucalyptus</i> (%)	Bagasse (%)	Mean (mm)	CV (%)
1	13	0.8	100	0	15.28	0.9
2	16	0.8	100	0	15.94	1.1
3	13	0.8	95	5	16.26	0.4
4	16	0.8	95	5	16.38	1.3
5	13	0.8	90	10	16.44	1.3
6	16	0.8	90	10	16.12	1.8
7	13	0.8	85	15	16.15	1.9
8	16	0.8	85	15	16.22	1.8
9	13	0.8	80	20	16.22	1.9
10	16	0.8	80	20	16.73	2.2
11	13	0.8	75	25	16.61	1.6
12	16	0.8	75	25	16.63	1.9

## Deflectometry measurements

### *Reflective coating transfer*

The deflectometry technique chosen in this work, although advantageous in measuring directly the slope field of the bent plate, requires a specular reflection of the surface of interest. Since the MDF panels do not have naturally a mirror-like surface, a thin reflective coating was transferred onto the surface. Different routes were followed in a trial-and-error approach. The most suitable result was reached by applying an epoxy resin coating. The implemented procedure follows closely the

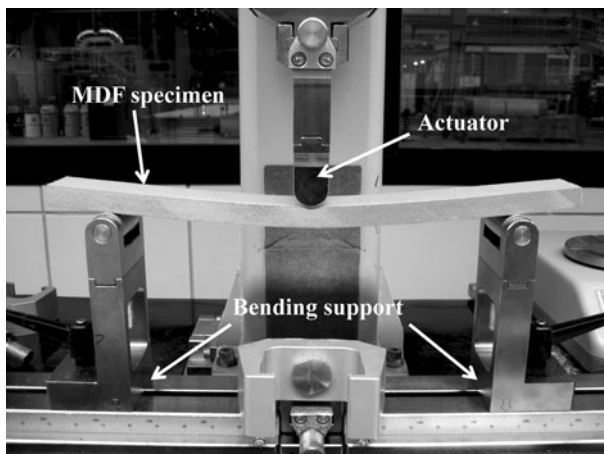


**Fig. 2** Set-up of the three-point bending mechanical test

one proposed by Kim et al. (2007) for specular reflection of polymer matrix composite plates. In order to guarantee the flatness of the resin coating, a counterpart glass surface was used as reference. Bee wax was carefully rubbed onto the glass surface, working as release agent. Care must be taken in order to avoid stains which will be visible in the coating, preventing the correct image formation of the grid pattern. The following procedure was implemented for achieving a specular surface on the MDF panels:

- roughening the surface of the panel (with 240 grit sandpaper) to remove small imperfections and to improve flatness;
- application of a paste (with the help of a metal spatula) in order to seal the surface panel and prevent absorption (drying for 24 h);
- roughening the surface of the panel (with 400 grit sandpaper) to remove most of the added mass and related imperfections;
- application of matt black synthetic spray paint in a uniform and thin layer (drying for 24 h), in order to enhance reflection at the top surface of the resin coating;
- pouring the surface with Surf Clear<sup>®</sup> epoxy resin (following the manufacturing procedure by SICOMIN, <http://www.sicomin.com>)—guarantees that all the panel surface is covered by the resin;
- applying the glass plate (reference surface) over the resin and applying some pressure to remove bubbles and correct spreading across the surface; applying weights over the surface to maintain proper contact between the glass and resin during cure;
- after curing (achieved in about 3 days at a temperature of 20 °C and 60 % relative humidity), carefully remove the glass plate. At the end, a thin reflective coating of about 0.5 mm is transferred onto the panel surface.

### Optical system

The pitch of the carrier grid used in the deflectometry technique was chosen taking into account the dimensions of the plate ( $a$ ,  $b$  in Fig. 1b), the pixel resolution of the digital camera ( $H$ ,  $V$ ) and number of pixels chosen for imaging a single period of the grid ( $N$ ). By choosing  $a = b = 370$  mm,  $H = 1,624$  pixel,  $V = 1,236$  pixel, and  $N = 10$  pixels/period, a grid pitch ( $p$ ) of 6 mm/period is calculated ( $p = 2p_p = 2N \times \text{Max}\{a/H, b/V\}$ , where  $p_p$  is the pitch of the grid image).

A crossed grid was printed on a matt, A0 paper ( $841 \times 1,189$  mm<sup>2</sup>) using a laser plotter. At the centre of the grid, a 25-mm-diameter hole was cut out, through which the optical system will observe the image of the grid reflected over the plate (Fig. 3d). The grid was then fixed on a rigid support to remain straight and motionless during the bending test (Fig. 3c). The distance between grid and plate was set to  $D = 2,810$  mm. In this configuration, the sensitivity of the deflectometry technique was  $s = 5,885$  rad/rad.

The images were recorded by an 8-bit Baumer<sup>®</sup> Optronic FWX20 camera (resolution of  $1,624 \times 1,236$  pixels) coupled with a Nikon<sup>®</sup> AF 28–105 f/3.5–4.5D

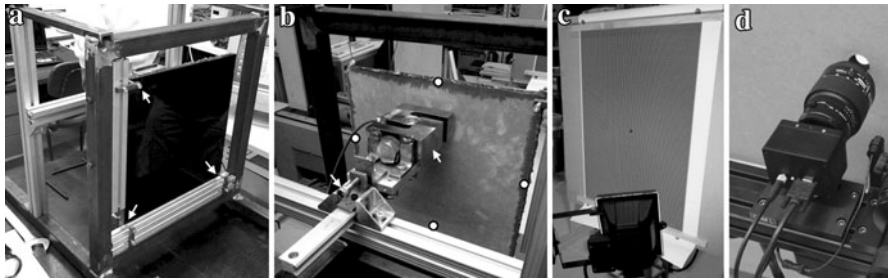


**Fig. 3** Plate bending test coupled with the deflectometry technique: **a** front fixture; **b** back fixture; **c** carrier grid; **d** camera-lens system

Zoom Nikkor lens. The support of the optical system was mounted on a tripod and positioned behind the grid at the hole level (Fig. 3d). Of course, at the hole location, there is no reflection of the grid, and therefore, no data will be available; nevertheless, this area only represents about 0.4 % of the region of interest. The lens was adjusted to focus on the virtual image of the grid reflected over the plate surface. The zoom lens (magnification factor) was set in order to guarantee a uniform spatial distribution of 10 pixels/period ( $N$ ) across the grid image ( $I$ ). By analysing the sub-image  $I/N$ , this condition is fulfilled when fringe bands are lost across the field of view (i.e. the number of fringes converges to zero). The lens aperture and exposure time were set to  $f/11$  and 40 ms, respectively. A LED Raylux® 25 lighting system was used for uniform illumination of the reference grid (Fig. 3c).

The resolution and the spatial resolution were proposed to characterise the measurements provided by the deflectometry technique (Surrel 2002). The resolution (i.e. the smallest measurable value) was estimated by carrying out motionless tests. This consisted in taking (at least) two images of the reflected grid without applying any deformation. By processing this pair of images, noisy maps were obtained from which a global estimate of the phase ( $\sigma_\phi$ ) and slope ( $\sigma_\alpha$ ) resolution can be determined on a statistical basis. The mean value over the difference of phase field can be associated with some bias or systematic error, whilst the standard deviation ( $\sigma_{\Delta\phi}$ ) is proportional to the phase resolution ( $\sigma_\phi$ ) by a factor of  $1/\sqrt{2}$ . The phase noise was found in the interval of  $2\pi/355 - 2\pi/680$  rad, being strongly correlated to the quality of the reflected image (resin coating transfer). On average, this corresponds to a slope resolution of  $\sigma_\alpha = \sigma_{\Delta\phi}/s = 3.1 \mu\text{radians}$  ( $\sigma_{\Delta\phi} = 0.018$  rad). Besides, no significant bias was found in these motionless measurements. The spatial resolution of the grid method (i.e. the smallest distance between two independent measurements) is approximately equal to the pitch of the grid. A pitch grid of 6 mm was used and since there is a magnification factor of 0.5 between the grid plane and the plate surface, a spatial resolution of  $\Delta x = 3$  mm was obtained.

### Plate bending test method

A fixture for the plate bending test was built up as shown in Fig. 3a, b. As schematically represented in Fig. 1b, the plate was vertically fixed at three points at

the corners (Fig. 3a). The load can be applied at any location at the back surface of the plate, generating heterogeneous curvature fields (Fig. 3b). Load case 1 (LC1) ( $F(0, b/2)$ , Fig. 1b) was applied in this work for identification of the two bending stiffness components, throughout Eq. (8). Load case 2 (LC2) ( $F(a, b/2)$ , Fig. 1b) was also carried out on the same plate in order to obtain an independent measurement of the shear modulus (Eq. 9). This redundant information can be used for checking the robustness of the method and verify the isotropy assumption in modelling the linear elastic behaviour of the MDF panels.

The load was measured by means of a 'S' type load cell of 5 kN mounted on a linear bearing (Fig. 3b). An acquisition system was used for load recording. The plate was deflected incrementally by manually advancing the loading system of 0.08 mm. Images of the grid, reflected on the deformed plate surface, were recorded at each stage. For LC1, about ten images were recorded leading to an applied load of almost 80 N, whilst for LC2 about 25 stages were needed to achieve this level of load (the number of images recorded during the bending tests was also limited by the fact that, at a certain level of deflection, the image reflected over the plate surface was too deformed or even out of the grid range). The maximum deflection applied to the plates was kept small with regard to the panel thickness (small displacement hypothesis).

## Results and discussion

### Identification of modulus of elasticity from three-point bending tests

The modulus of elasticity of the MDF panels was determined from standard three-point bending tests according to Eq. (10). These results are summarised in Table 3. The scatter on the mean values associated with these measurements (quantified by the coefficient of variation (CV)) was in the range of 8–13 %.

In a further analysis, the influence of the percentage of sugarcane bagasse particles (Table 2) on the modulus of elasticity ( $E$ ) of the panels is shown in Fig. 9a. As can be concluded from the linear regression analysis of this set of data (coefficient of correlation of  $R = 0.115$ ), a poor statistical correlation was found between  $E$  and the percentage of sugarcane bagasse particles. A mean value of  $3,393 \text{ N/mm}^2$  with a CV of 5.86 % was obtained over all treatments. By itself, this result justifies the utilisation of waste sugarcane bagasse in the MDF manufacturing process bringing added value to this raw material.

### Identification of stiffness components from plate bending tests

#### *Phase and slope fields calculation*

The grid images recorded during the plate bending tests were firstly processed for evaluating the phase fields. These phase maps encode the position of the carrier grid for each loading stage. To start with, the images of the crossed grid were split into two sets of images with only vertical and horizontal lines, respectively. This pre-

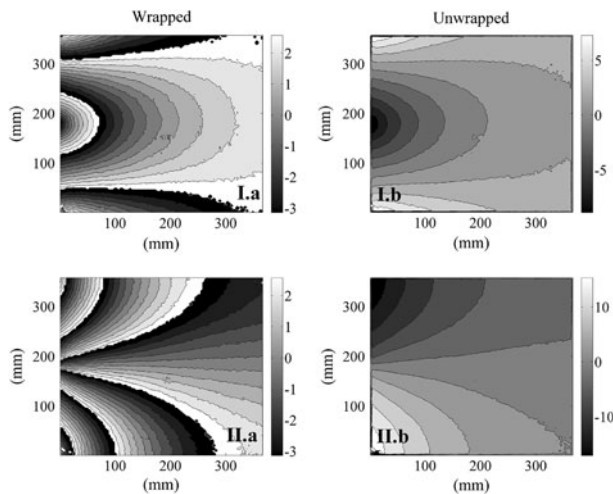


**Fig. 4** **a** Wrapped and **b** unwrapped difference of phase field along the (I)  $x_1$  and (II)  $x_2$  directions (load case 1,  $F = 45.1$  N) (unit: radian)

processing step was required to evaluate the two components of the phase (slope) field in a coordinate system defined by the grid lines. For this purpose, the images were filtered by a triangular window kernel of length  $2N-1$  pixels (where  $N$  is the number of pixels sampling one period). The phase components corresponding to each image were then determined by means of a phase-shifting method (Surrel 1999). This calculation yields a phase modulo  $2\pi$ , as shown in Fig. 4a (obtained at a load of 45.1 N for load case LC1 (Fig. 1b) and for the MDF plate with 13 % of resin content and 0 % of sugarcane bagasse particles (Table 2)). A phase-unwrapping algorithm was then required to remove  $2\pi$  jumps and thus provide continuous kinematic fields. The Goldstein method was used in this work for phase unwrapping (Ghiglia and Pritt 1998). A point near a support of the plate was used for starting the phase-unwrapping process. Even if the slope at this point is not strictly zero, this bias does not affect the curvature field reconstruction because this constant value vanishes in the differentiation process. The resulting difference of phase fields is shown in Fig. 4b. Figure 5a represents the corresponding components of the slope field (Eq. 3): (I)  $\theta_1(x_1, x_2)$  and (II)  $\theta_2(x_1, x_2)$ .

### Curvature field reconstruction

The slope fields were numerically differentiated in order to determine the curvature fields at the surface of the deformed plate. For this purpose, a global polynomial least-squares approach was used. The main advantages of polynomial approximation are: (1) the simplicity of the approach, (2) the possibility to give different weights to each point and therefore discard erroneous data (i.e. points where data are too noisy or missing), (3) the interpolation or extrapolation of the slope value at points where no information is initially available. On the other hand, some drawbacks exist: (1) the instability of the reconstruction of the curvature fields,

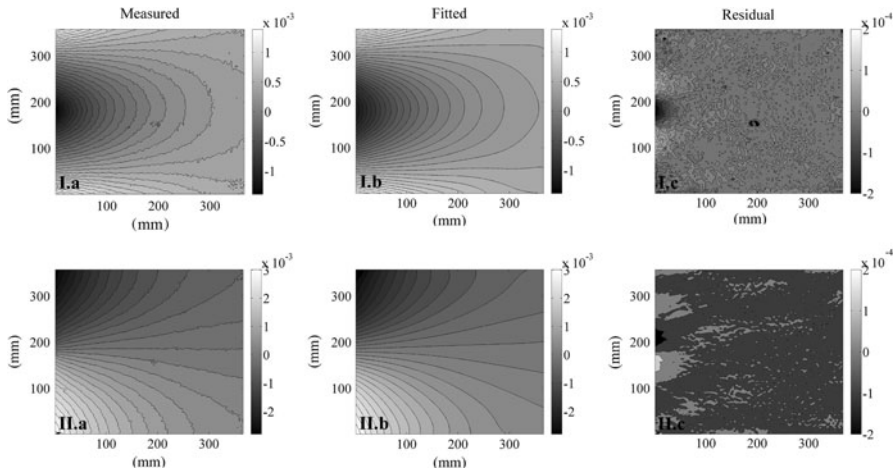


**Fig. 5** (I)  $\theta_1(x_1, x_2)$  and (II)  $\theta_2(x_1, x_2)$  slope fields: **a** measured, **b** fitted (polynomial order 8), **c** residual (load case 1,  $F = 45.1$  N) (unit: radian)

namely at the edges of the region of interest when high-degree polynomials are used and (2) the propagation of local errors over the whole field because of the global reconstruction scheme of the polynomial basis functions.

A key issue in the least-squares polynomial approximation is the selection of the polynomial order. This value was selected based on two complementary analyses. Firstly, the convergence of the standard deviation of the residual maps—obtained by subtracting measured and approximated slope fields—with regard to the polynomial order, varying from 3 up to 20, was analysed (Fig. 6a). Secondly, the convergence of the identified bending stiffness values with regard to the polynomial order was checked (Fig. 6b). From these analyses, a polynomial order equal to 8 was chosen as a compromise between noise filtering (higher orders) and reconstruction errors (lower orders). The fitted and residual slope fields obtained from this approach are shown in Fig. 5b and c, respectively. The residual maps indicate a good reconstruction almost within the whole region of interest; the highest differences

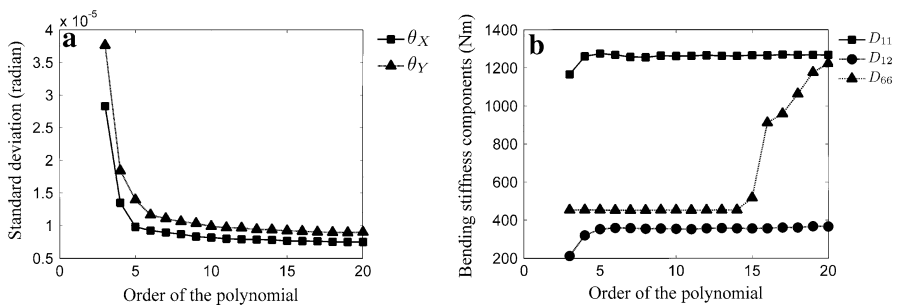


**Fig. 6** **a** Standard deviation of residual maps obtained by subtracting measured and polynomial approximated slope fields; **b** identified bending stiffness components both as a function of the polynomial order



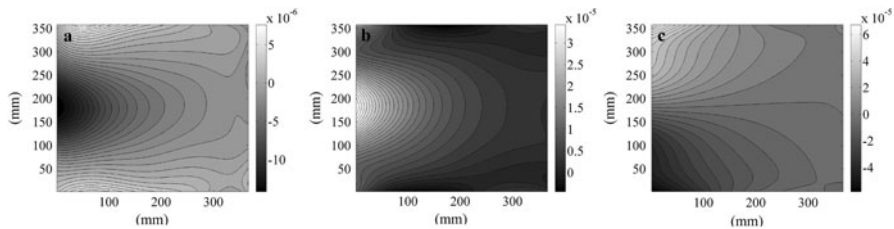


**Fig. 7** Curvature fields: **a**  $K_{11}(x_1, x_2)$ , **b**  $K_{22}(x_1, x_2)$  and **c**  $K_{12}(x_1, x_2)$  (load case 1,  $F = 45.1$  N) (unit:  $\text{mm}^{-1}$ )

occurring near the region of applied punctual load. From the approximated slope fields, the curvature fields were then determined by differentiation. Figure 7 shows the reconstructed curvature fields obtained at a load of 45.1 N (LC1 in Fig. 1b) and for a MDF plate with 13 % of resin content and 0 % of sugarcane bagasse particles (Table 2).

An analysis was also performed consisting of the reconstruction of the curvature fields based on images recorded without applying any deformation to the plate (motionless tests). As done before for the phase and slope fields (Sect. “Optical system”), this analysis can yield an estimate of the curvature resolution. By processing this set of images, noisy curvature maps were obtained from which a mean value of about  $10^{-10} \text{ mm}^{-1}$  and a standard deviation (resolution) of  $10^{-8} \text{ mm}^{-1}$  (the associated strain resolution is about  $0.076 \mu\text{def}$ ) were calculated. Finally, for the sake of comparison with regard to the least-squares polynomial approximation, finite differences were also applied to the (noisy) slope maps in order to reconstruct the curvature fields. With this numerical differentiation technique, however, a curvature resolution one order of magnitude higher (standard deviation of  $10^{-7} \text{ mm}^{-1}$ ) was systematically obtained.

### Bending stiffness components evaluation

The curvature fields were integrated over the plate domain and input, together with load and dimensions of the plate, into the VFM for identification of the bending

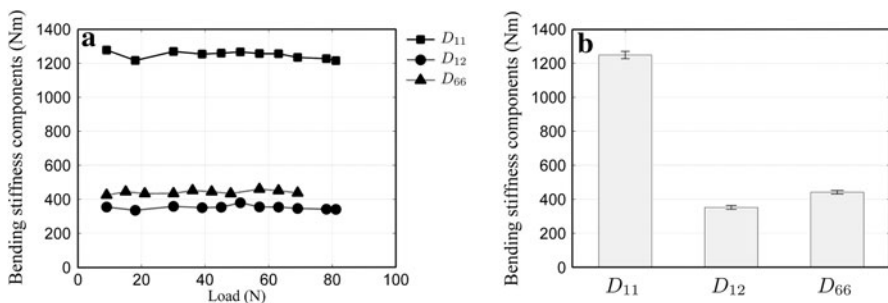


**Fig. 8** **a** Variation of bending stiffness components as a function of the applied load; **b** evaluation of mean and standard deviation values

**Table 3** Characterisation of MDF by three-point and plate bending tests

No	Three-point bending tests		Plate bending tests						
	$E$ (CV) (N/mm <sup>2</sup> )	$G^{(a)}$ (N/mm <sup>2</sup> )	$D_{11}$ (N m)	$D_{12}$ (N m)	$D_{66}$ (N m)	$\nu^{(b)}$ (–)	$E^{(c)}$ (N/mm <sup>2</sup> )	$G^{(d)}$ (N/mm <sup>2</sup> )	$G^{(e)}$ (N/mm <sup>2</sup> )
1	3,398 (12.9 %)	1,325	1,256	355	434	0.28	3,887	1,515	1,459
2	3,643 (8.0 %)	1,475	1,499	353	552	0.24	4,195	1,698	1,636
3	3,067 (11.9 %)	1,239	1,351	321	495	0.24	3,558	1,437	1,383
4	3,533 (10.8 %)	1,381	1,418	396	538	0.28	3,570	1,395	1,469
5	3,256 (10.2 %)	1,289	1,324	349	492	0.26	3,328	1,317	1,329
6	3,732 (9.4 %)	1,490	1,368	345	522	0.25	3,670	1,466	1,495
7	3,419 (11.2 %)	1,339	1,240	343	471	0.28	3,262	1,277	1,341
8	3,543 (11.8 %)	1,434	1,361	320	536	0.24	3,615	1,463	1,507
9	3,213 (8.3 %)	1,295	1,250	300	474	0.24	3,312	1,335	1,334
10	3,408 (12.9 %)	1,408	1,368	287	558	0.21	3,352	1,385	1,429
11	3,345 (10.8 %)	1,388	1,375	282	520	0.21	3,448	1,430	1,362
12	3,158 (9.1 %)	1,254	1,293	335	529	0.26	3,147	1,250	1,380
Mean	3,393	1,360	1,342	332	510	0.25	3,529	1,414	1,427
CV (%)	5.86	6.11	5.62	9.70	7.30	10.27	8.31	8.51	6.39

<sup>(a)</sup>  $G = E/2(1 - \nu)$ , by taking  $\nu = D_{12}/D_{11}$  (from plate bending tests)

<sup>(b)</sup>  $\nu = D_{12}/D_{11}$

<sup>(c)</sup>  $E = (12/h^3)(1 - \nu^2)D_{11}$  ( $h$  in Table 2)

<sup>(d)</sup>  $G = (6/h^3)(1 - \nu)D_{11}$

<sup>(e)</sup>  $G = (12/h^3)D_{66}$

stiffness components (Eqs. 8 and 9). As an example, the evaluation of the bending stiffness components as a function of the applied load is shown in Fig. 8a. In this case,  $D_{11}$  and  $D_{12}$  were determined from load case 1 ( $F(0, b/2)$ ) in Fig. 1b), whilst  $D_{66}$  was identified on the same MDF panel but performing an independent test

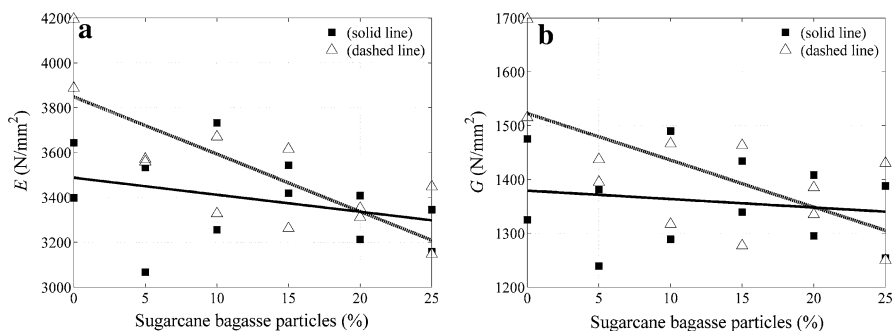


**Fig. 9** Variation of (a) modulus of elasticity ( $E$ ) and (b) shear modulus ( $G$ ) as a function of percentage of sugarcane bagasse particles ( $p$ ) (filled square—three-point bending test:  $E = -7.6p + 3487.7$  ( $R^2 = 11.5\%$ ),  $G = -1.6p + 1379.3$  ( $R^2 = 2.8\%$ ); open triangle—plate bending test:  $E = -25.6p + 3848.2$  ( $R^2 = 60.5\%$ ),  $G = -8.7p + 1522.7$  ( $R^2 = 41.6\%$ ))

corresponding to load case 2 ( $F(a, b/2)$  in Fig. 1b). Figure 8b represents the mean and the standard deviation of the stiffness components determined at each loading step. As can be seen, the results are reasonably stable and with low scatter.

The set of bending stiffness values ( $D_{11}$ ,  $D_{12}$  and  $D_{66}$ ) of the MDF panels identified from the proposed data reduction scheme are reported in Table 3. The mean values of the stiffness, among all treatments, were also evaluated. For the sake of comparison with regard to standard tests or values reported in the literature, these stiffness components were converted into engineering constants according to constitutive relationships. To start with, *Poisson's* ratio was determined according to the relationship  $\nu = D_{12}/D_{11}$  (Table 3). A mean value of  $\nu = 0.25$  was found among all treatments (a C.V. of about 10 % was obtained, which is not surprising since this is normally a difficult quantity to identify experimentally). This value is within the range of 0.14–0.28 reported in literature for this type of material (Moboru and Taeko 2004). Assuming this value of *Poisson's* ratio and considering the thickness of the plates ( $h$  values in Table 2), a conversion for both the modulus of elasticity ( $E$ ) and the shear modulus ( $G$ ) was provided (Table 3). The modulus of elasticity measured from the plate bending tests was generally slightly higher than the one measured from classical three-point bending tests but still in the same order of magnitude (on average a relative difference of 3.8 % was obtained). Deformation of the machine is probably negligible, but not the indentation effect. There may also be some clearance slack at the early stages of the test. This is consistent with the fact that the modulus is systematically underestimated with the standard test.

Assuming isotropy, reference values of the shear modulus ( $G = E/2(1 + \nu)$ ) were also estimated from the modulus of elasticity measured by three-point bending tests (Table 3). These values were then compared with shear modulus determined independently from both  $D_{11}$  (LC1:  $G = (6/h^3)/(1 - \nu)D_{11}$ ) and  $D_{66}$  (LC2:  $G = (12/h^3)D_{66}$ ) provided from the plate bending tests. Firstly, by comparing the shear modulus measured from LC1 and LC2, it can be concluded that they correspond to the same mean value according to the  $t$  test for equality of means of two samples (same variance) at a 95 % confidence level. This analysis represents an independent confirmation of the isotropy assumption in modelling the MDF panels. Secondly, the shear modulus obtained from the plate bending tests compared relatively well with the reference value determined from modulus of elasticity provided by the three-bending tests (relative difference of about 4–5 %).

The evaluation of  $E$  and  $G$  measured from both three-point and plate bending tests with regard to the percentage of sugarcane bagasse particles (Table 2) is shown in Fig. 9. Both elastic and shear moduli determined from three-point bending tests show little correlation with the percentage of sugarcane bagasse particles. These correlations increased when taking elastic and shear moduli obtained from the plate bending tests, from which a coefficient of determination ( $R^2$ ) of 60.6 % and 41.6 % was found, respectively. This latter result follows the previous observation showing that the properties of the MDF panels degrade by increasing the fraction of sugarcane bagasse particles in the MDF manufacturing (Belini et al. 2012). In this latter study, the percentage of sugarcane bagasse particles ranged from 0 % up to 100 % with steps of 25 %.

## Conclusion

In this work, a new data reduction scheme to identify the bending stiffness components of MDF panels from a single plate bending test was proposed. MDF panels consisting of different volume fractions of waste sugarcane bagasse particles and *Eucalyptus grandis* fibres were tested in this work. With regard to standard three-point bending tests usually carried out to evaluate the modulus of elasticity of MDF panels, the major advantage of the proposed approach is the full characterisation of the bending stiffness matrix (modulus of elasticity, *Poisson's* ratio and shear modulus) from a single-test configuration. The approach couples full-field slope measurements with an inverse identification method. The full-field measurements were provided by the deflectometry (reflected grid) technique. An experimental procedure was proposed for coating the MDF surface with a reflective epoxy resin. The material characterisation was then achieved by implementing the virtual fields method under the framework of the Kirchhoff–Love plate bending theory.

The bending stiffness (or engineering constant) values obtained from the proposed data reduction approach were within less than 4 % from results determined from standard three-point bending tests and from reference values reported in the literature for this type of material. Besides, from the proposed method, it was possible to check the isotropy assumption in modelling the MDF panel (i.e. random distribution of fibres within the panel), by carrying out an independent bending test on the same plate (with another suitable loading case) and by choosing a constant twisting virtual field in the virtual fields method.

The elastic and shear moduli showed a weak (from three-point bending tests) or moderated (from plate bending tests) correlation with regard to the fraction of sugarcane bagasse particles in the MDF panels (in the range from 0 to 25 % with steps of 5 %). This result points out the interest of using some percentage of recycled wood material fibres for the production of this type of wood products in a perspective of better preservation and management of the available agricultural and forestry resources.

As future work, a more general implementation of the VFM for plate bending tests will be targeted by using special and optimised virtual fields (Syed-Muhammad et al. 2008). This extension, with regard to the methodology presented in this work, can eventually allow the characterisation of spatial variation of elastic properties across the plate. This could be particularly relevant when testing, for instance, wooden plates cut from the centre to the periphery of the stem, since significant variability is expected to occur along this direction (Machado and Cruz 2005; Xavier et al. 2009).

**Acknowledgments** The authors would like to acknowledge the São Paulo Research Foundation (FAPESP), the programs CAPES-GRICES and *Ciência 2008* of the Foundation of Science and Technology of Portugal (FCT) for financial support. We also thank São Manoel Sugar Factory S.A. (Brasil) for support in the MDF manufacturing process. Finally, we thank Joaquim Moura and Cristóvão Santos for helping in the plate bending fixture set-up.

## References

- Avril S, Grédiac M, Pierron F (2004) Sensitivity of the virtual fields method to noisy data. *Comput Mech* 34(6):439–452
- Avril S, Bonnet M, Bretelle AS, Grédiac M, Hild F, Ienny P, Latourte F, Lemosse D, Pagano S, Pagnacco E, Pierron F (2008) Overview of identification methods of mechanical parameters based on full-field measurements. *Exp Mech* 48(4):381–402
- Belini U, Tomazello Filho M, Louzada J, Rodrigues J, Astolphi J (2012) Pilot study for MDF manufacture from sugarcane bagasse and Eucalyptus fibers. *Eur J Wood Prod* 70(4):537–539
- EN 310 (1993) Wood-based panels, determination of modulus of elasticity in bending and bending strength. European Committee for Standardization, Brussels, Belgium
- Ghiglia D, Pritt M (1998) Two-dimensional phase unwrapping: theory, algorithms, and software. Wiley, USA
- Grédiac M (2004) The use of full-field measurement methods in composite material characterization: interest and limitations. *Compos A Appl Sci Manuf* 35(7–8):751–761
- Grédiac M, Toussaint E, Pierron F (2003) Special virtual fields for the direct determination of material parameters with the virtual fields method. 3- Application to the bending rigidities of anisotropic plates. *Int J Solids Struct* 40(10):2401–2419
- Grédiac M, Pierron F, Avril S, Toussaint E (2006) The virtual fields method for extracting constitutive parameters from full-field measurements: a review. *Strain* 42(4):233–253
- Kim JH (2008) Identification of the local stiffness reduction of damaged composite plates using the virtual fields method. PhD thesis, Art et Métiers ParisTech Châlons-en-Champagne, France
- Kim JH, Pierron F, Grédiac M, Wisnom M (2007) A procedure for producing reflective coatings on plates to be used for full-field slope measurements by a deflectometry technique. *Strain* 43(2): 138–144
- Machado J, Cruz H (2005) Within stem variation of maritime pine timber mechanical properties. *Holz Roh Werkst* 63(2):154–159
- Moboru S, Taeko S (2004) *Poisson's* ratio of wood-based panels and *Poisson's* effect of hygroscopic linear expansion under a uniaxially dimensional restraint. *J Soc Mat Sci* 53(4):396–401
- Müller U, Sretenovi A, Vincenti A, Gindl W (2005) Direct measurement of strain distribution along a wood bond line. Part 1: shear strain concentration in a lap joint specimen by means of electronic speckle pattern interferometry. *Holzforschung* 59(3):300–306
- Pierron F (2009) A novel method for measuring the through-thickness shear moduli of anisotropic plates from surface deformation measurements. *Compos A Appl Sci Manuf* 40(12):1815–1825
- Pierron F, Grédiac M (2012) The virtual fields method. Springer, New York
- Surrel Y (1999) Fringe analysis. In: Rastogi P (ed) *Photomechanics* (topics in applied physics). Springer, Berlin, pp 57–104
- Surrel Y (2002) Some metrological issues in optical full-field techniques. *Proc SPIE* 4777:220–231
- Surrel Y (2004) Deflectometry: a simple and efficient noninterferometric method for slope measurement. In: Xth SEM International congress on experimental mechanics, society for experimental mechanics, 7–10 June in Costa Mesa, California, USA
- Syed-Muhammad K, Toussaint E, Grédiac M, Avril S, Kim J (2008) Characterization of composite plates using the virtual fields method with optimized loading conditions. *Compos Struct* 85(1):7082
- Williamson TG (2002) *APA engineered wood handbook*. McGraw-Hill, USA
- Xavier J, Avril S, Pierron F, Morais J (2009) Variation of transverse and shear stiffness properties of wood in a tree. *Compos A Appl Sci Manuf* 40:1953–1960
- Xavier J, de Jesus A, Morais J, Pinto J (2012) Stereovision measurements on evaluating the modulus of elasticity of wood by compression tests parallel to the grain. *Constr Build Mater* 26(1):207–215
- Zhou C, Dai C, Smith G (2011) Modeling vertical density profile formation for strand-based wood composites during hot pressing: part 2. Experimental investigations and model validation. *Compos B Eng* 42(6):1357–1365